Multi-Objective Four-Dimensional Vehicle Motion Planning in Large Dynamic Environments

Paul P.-Y. Wu, *Member, IEEE*, Duncan Campbell, *Member, IEEE*, and Torsten Merz, *Member, IEEE*

***Abstract*—This paper presents Multi-Step A* (MSA*), a search algorithm based on A* for multi-objective 4-D vehicle motion planning (three spatial and one time dimensions). The research is principally motivated by the need for offline and online motion planning for autonomous unmanned aerial vehicles (UAVs). For UAVs operating in large dynamic uncertain 4-D environments, the motion plan consists of a sequence of connected linear tracks (or trajectory segments). The track angle and velocity are important parameters that are often restricted by assumptions and a grid geometry in conventional motion planners. Many existing planners also fail to incorporate multiple decision criteria and constraints such as wind, fuel, dynamic obstacles, and the rules of the air. It is shown that MSA* finds a cost optimal solution using variable length, angle, and velocity trajectory segments. These segments are approximated with a grid-based cell sequence that provides an inherent tolerance to uncertainty. The computational efficiency is achieved by using variable successor operators to create a multiresolution memory-efficient lattice sampling structure. The simulation studies on the UAV flight planning problem show that MSA* meets the time constraints of online replanning and finds paths of equivalent cost but in a quarter of the time (on average) of a vector neighborhood-based A*.**

***Index Terms*—Heuristic algorithms, multi-objective decision making, path planning, unmanned aerial vehicles (UAVs).**

I. Introduction

An IMPORTANT component in the operation of vehicles in large 4-D (three spatial and one time dimensions) dynamic environments is motion planning. This involves finding an optimal (least cost) or near-optimal sequence of 4-D states that connect the initial vehicle state to a desired goal state [1]. For many applications, it is necessary to plan offline (e.g., prepare a mission plan for regulatory approval) and replan online when the planning assumptions are invalidated by in-mission changes. The research is principally motivated by the operation of robotic vehicles, namely autonomous unmanned aerial vehicles (UAVs) and, equivalently, autonomous underwater vehicles (AUVs).

UAVs and AUVs are characterized by the following: 1) operation in large outdoor environments; 2) movement in three dimensions (x, y, z); 3) uncertain and dynamic operating environment; 4) presence of environmental forces that affect motion (winds or currents); and 5) differential constraints on movement [2], [3]. Because of 2) and 3), the planning space must be 4-D. Note that a dynamic environment refers not only to moving obstacles but also to changing weather conditions. This paper mitigates the uncertainty inherent in a dynamic environment through online replanning and incorporation of tolerances in the planning process. Online replanning in this paper refers to the execution of a search (i.e., replan) during a mission. It is assumed that the inputs to the planner are constant during a replan; hence, there is significant time pressure on the replanning process.

The motion plan is constrained by vehicle dynamics (such as maximum climb/ascent rate), environmental constraints (e.g., static and dynamic obstacles and wind/current), and rules of the air/sea. In addition, the planned path must satisfy (and optimize for) multiple possibly conflicting objectives such as fuel efficiency and flight time. Due to the "curse of dimensionality" [4], it is not computationally feasible to plan in a high dimensional search space consisting of all the aforementioned variables. It is common, instead, to plan the path in the world space (x, y, z, t) [1] by aggregating the decision variables into a single nonbinary cost term [4]. This planning problem is a type of weighted region path planning [5]. An optimal path search algorithm like A* [6] is needed as the shortest path is not necessarily the least cost path.

One of the unique UAV/AUV characteristics listed earlier is the presence of wind (or currents). These constrain vehicle movements affect the travel time and fuel consumption. In the presence of wind, it is particularly important to have high track-angle resolution as low track-angle resolution can result in suboptimal paths that contain spurious turns [7], [8]. This is a shortcoming of conventional search grids as the track angle is in increments of 45°.

Note that the 4-D motion planning as described here should not be confused with trajectory planning, which finds a path expressed in terms of the degrees of freedom of the vehicle and velocity/angle rates [1]. Instead, a 4-D motion plan comprises a georeferenced sequence of 3-D waypoints and the desired track velocities between them. In this paper, such tracks are also equivalently referred to as trajectory segments.

This paper presents Multi-Step A* (MSA*), a method for the 4-D vehicle motion planning based on variable length, angle, and velocity trajectory segments. Section II reviews

Manuscript received June 8, 2009; revised January 12, 2010 and April 8, 2010; accepted April 12, 2010. Date of publication September 16, 2010; date of current version May 18, 2011. This work was supported in part by the Australian Research Centre for Aerospace Automation and in part by the Information and Communication Technologies Centre Commonwealth Scientific and Industrial Research Organisation Top-Up Scholarship. This paper was recommended by Associate Editor E. Tunstel.

P. P.-Y. Wu is with the Australian Research Centre for Aerospace Automation, Queensland University of Technology, Brisbane 4000, Australia (e-mail: p.wu@qut.edu.au).

D. Campbell is with the School of Engineering Systems and the Australian Research Centre for Aerospace Automation, Queensland University of Technology, Brisbane 4000, Australia (e-mail: da.campbell@qut.edu.au).

T. Merz is with the Information and Communication Technologies Centre, Commonwealth Scientific and Industrial Research Organisation, Brisbane 4069, Australia (e-mail: torsten.merz@csiro.au).

Color versions of one or more of the figures in this paper are available online at http://ieeexplore.ieee.org.

Digital Object Identifier 10.1109/TSMCB.2010.2061225

existing path planning techniques. Based on A* [6], the proposed method is presented in Section III and shown to be cost optimal. To take advantage of the variable trajectory segments, a memory- and time-efficient multiresolution lattice structure is proposed in Section IV. A simulation study of MSA* for the UAV flight planning task is discussed in Section V. Analysis of the simulation results and a comparison of MSA* with existing works are discussed in Section VI.

II. Existing Work

Much of the recent work in vehicle planning has focused on techniques in computational geometry using a grid [7]–[16]. However, a shortcoming of many grid-based approaches (e.g., [14] and [16]) is that the resultant path is confined to track angles that are multiples of 45°. As a result, the path can be suboptimal and may contain spurious turns [7], [8]. A lack of regular high-resolution track angles also affects methods based on Voronoi graphs (e.g., [11] and [17]), methods that use probabilistic sampling (e.g., [18] and [19]), and, generally, methods where the path angles are not considered (e.g., [15] and [20]). A review of motion-planning algorithms is provided hereinafter for the methods that address the requirements of the vehicle motion planning vis-a-vis the track-angle problem, wind/current effects, and multi-objective optimization.

A. Methods With High-Resolution Track Angles

A number of grid-based methods determine the track angle in continuous space instead of sampling from predefined discrete track angles. However, geometry-based methods in 2-D or 3-D (or even 4-D) space, such as Theta* [8] and $A_{3\mathrm{D}}$ [15], do not find the optimal path. Field D* [7] and 3-D Field D* [13] find the optimal path, but both assume *a priori* knowledge of cell costs (which are used to derive the track angle and track cost). This approach is infeasible in a 4-D search space as the cost is dependent on the track angle. Nevertheless, it is shown that a multiresolution search space can be used to mitigate the memory and time complexity of the motion planning [1], [7], [9], [13].

Pivtoraiko and Kelly [12] present an alternate method that provides regular high-resolution track angles by defining a successor operator (i.e., parent child cell relationships) that has a predetermined number of successors at selected track angles. Like Theta*, parent cells are not necessarily adjacent to child cells, hence, the notion of a vector neighborhood [1]. However, the method is formulated for 2-D vehicle planning with no consideration for winds/currents.

The framed quad/octree [9] enables the high-resolution track angles by placing sample nodes on the boundaries of each quad/octree decomposed cell. However, the transitions between cells are again limited to increments of 45°. Additionally, neither [9] nor [12] consider the wind effects.

A number of existing planners model the wind effects using weighted polygonal (or polyhedral) shaped regions [21]–[24]. However, these methods do not consider the multiple objectives and are not suited for planning in a dynamic environment. This is a similar shortcoming of AUV [14] and UAV [10] motion planners that incorporate wind.

Finally, there are motion planners based on artificial evolution (e.g., [10], [18], and [19]) that plan in continuous space. A shortcoming of evolutionary algorithms is the inability to specify bounds on the computation time or solution optimality [25]. This can be problematic for the online replanning (due to real-time constraints) and for applications where determinism is a regulatory requirement (e.g., DO178-B [26] for aviation software).

B. Multi-Objective Planning Algorithms

None of the previously quoted methods explicitly address the requirement of optimizing for multiple decision objectives, although many incorporate the multiple path constraints (e.g., water currents and vehicle dynamics in [14]). Examples of explicit multi-objective planning algorithms can be found in the study of hazardous materials transportation [27]. These algorithms combine a multi-objective decision function (typically, a weighted sum) with a graph search algorithm (such as A* or Dijkstra's algorithm) on a grid [27]–[30] (refer to [31] for a description). This methodology is also used by Gu [11] for a bi-objective (risk and fuel objectives) UAV motion planner. These multi-objective planning algorithms (e.g., [11] and [27]–[30]) almost universally adopt a global planning approach where the track cost is calculated at a search time (much like a lazy probabilistic roadmap [1]).

An alternative approach to multi-objective path planning is to use a multi-objective search algorithm like [17] and [32]. However, these algorithms are computationally expensive and, in the case of [32], restricted to acyclic graphs; note that graphs derived from grids are cyclic.

A similar direct approach to multi-objective path planning is logic-based planning. Three candidate approaches include the hierarchical task network (HTN) [33], temporal action logic [34], and multiflip satisfiability solver, which evaluates nonadjacent neighbors in logic space [35]. An application of the HTN to indoor robot navigation is described in [36]. However, the logic-based motion planning is generally computationally expensive, and the resultant plan is typically nonoptimal [1], [33].

It can be seen that the existing methods do not fully address the multi-objective vehicle motion-planning problem.

III. MSA*

The planning task is defined as finding a path P through a roadmap S, starting at node s_0 and terminating at node s_G. Each node $s \in S$ is located at the center of a 4-D rectangloid cell defined in the world space $W(x, y, z, t)$. Assuming a regular grid sampling of the search space, each node s maps uniquely to a cell in W. Thus, s refers simultaneously to both the cell and the node located in the center of each cell. The global planning approach described in Section II is adopted, whereby the tracks are evaluated online and the initial roadmap is not explicitly represented (like with [20]). Instead, the roadmap is defined implicitly through a successor (or neighborhood) operator Γ where, for a given source (or parent) node s, $\Gamma(s)$ denotes a set of cell sequences $\gamma_{s'} \in \Gamma(s)$ which begin at s and terminate at the successor (or child) node $s' \in S'$.

Consider the modeling of a vector neighborhood like [12] where s' does not necessarily lie adjacent to s. The successor operator is assumed to denote a linear trajectory/track connecting the center of cell s to the center of cell s' (refer to Fig. 1). It is assumed that the turns (possibly required between tracks)

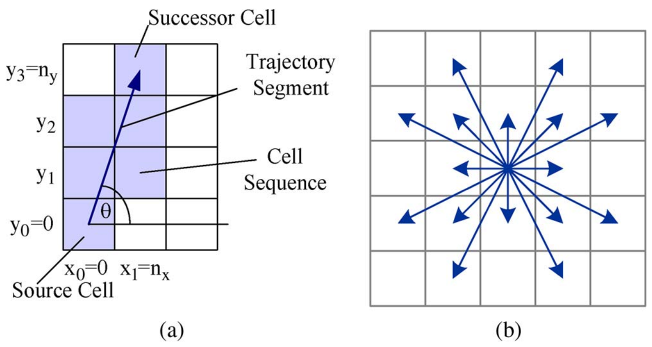

Fig. 1. Successor operator illustration. (a) Single 2-D trajectory segment and the corresponding cell sequence. (b) Example 2-D successor operator showing individual trajectory segments. Note that the trajectory segment terminates in the center of the successor cell, which is not necessarily adjacent to the source cell.

have a negligible impact on the overall path in terms of travel time and fuel consumption. For each successor s', the trajectory intersects a sequence of cells between s and s'

$$\gamma_{s'} = \{s_{j+m-1} = s' \| s_j = s, \ldots, s_{j+m-2}\} \tag{1}$$

where $s_j, \ldots, s_{j+m-1}$ is a sequence of m cells and $\|$ denotes a conditional dependence, i.e., $s_{j+m-1} \| s_j, \ldots, s_{j+m-2}$ is interpreted as cell s_{j+m-1} via a sequence of cells $s_j, \ldots, s_{j+m-2}$. In the ensuing sections, Γ is derived for a 3-D world ($\Gamma_{3\mathrm{D}} \in \Gamma$; see Section III-A) and then extended to four dimensions (see Section III-B). This is possible as the search dimensions are orthogonal.

A. Multistep Three-Dimensional Successor Operator

As illustrated in Fig. 1(a), it is possible to determine the horizontal track angle θ and slope from the endpoints of each trajectory segment. The vertical track angle ϕ and slope can be similarly determined for a 3-D trajectory segment. In aviation, the horizontal and vertical track angles are referred to as the ground track angle and flight path angle, respectively. Note that the vertical slope is given by the climb/descent rate and the ground speed. The angles can then be used to determine the cells that intersect the track using a variant of Bresenham's pixel algorithm [37]. Note that, because the vehicle controller has a nonzero trajectory tracking error, it is necessary to include cells whose edges/corners touch the trajectory line. This prevents the possibility of the vehicle squeezing through an infinitesimally small gap or "brushing past" as an obstacle. Doing so provides an intrinsic tolerance to the navigational and controller uncertainty as there is always a safety margin between the trajectory segment and the boundaries of a cell.

Using Bresenham's [37] line drawing concept, the determination of a 3-D cell sequence is based on the displacement (n_x, n_y, n_z) of the successor cell from the source in terms of the number of cells in the x, y, and z dimensions, respectively. This sequence is invariant to the physical dimensions of each cell but assumes regular cells. The 3-D line equations are

$$\begin{cases} y = \frac{n_y}{n_x}x, \ z = \frac{n_z}{n_x}x, & \text{if } |n_x| \geq |n_y|, \ |n_x| \geq |n_z| \\ x = \frac{n_x}{n_y}y, \ z = \frac{n_z}{n_y}y, & \text{if } |n_x| < |n_y|, \ |n_y| \geq |n_z| \\ x = \frac{n_x}{n_z}z, \ y = \frac{n_y}{n_x}x, & \text{if } |n_x| \geq |n_y|, \ |n_x| < |n_z| \\ y = \frac{n_y}{n_z}z, \ x = \frac{n_x}{n_y}y, & \text{if } |n_x| < |n_y|, \ |n_y| < |n_z|. \end{cases} \tag{2}$$

Note that, as is done in [37], line symmetry properties are exploited to avoid slopes greater than one. The cells in the sequence are determined by selecting and then applying the appropriate equation in (2) for each successor (n_x, n_y, n_z). The equation is evaluated at the midpoints between cells, i.e., $0.5, 1.5, \ldots, n - 0.5$ cell widths. If the midpoint lies on an edge, the cells that share that edge are included in the cell sequence. If the midpoint intersects a corner point, all cells that share that corner point are included. This produces a cell sequence that has Manhattan stepping with a nonzero spacing between the trajectory segment and cell boundaries. The horizontal and vertical track angles θ and ϕ can be calculated from the displacement, as shown in (3) and (4), respectively

$$\theta = \arctan\left(\frac{n_x \delta x}{n_y \delta y}\right) \tag{3}$$

$$\phi = \arctan\left(\frac{n_z \delta z}{\sqrt{(n_x \delta x)^2 + (n_y \delta y)^2}}\right) \tag{4}$$

where δx, δy, and δz correspond to the x, y, and z dimensions of each cell, respectively. Note that, as Γ is specified *a priori*, there is no need to optimize the cell sequence generation algorithm.

Consider the design of $\Gamma_{3\mathrm{D}}$. From (3) and (4), it can be seen that arbitrary track angles are possible; however, this can result in successors that are displaced by a large cell distance (n_x, n_y, n_z) from s. For example, a horizontal track-angle resolution (i.e., the maximum angular distance between sample points) of 45° is achieved with a maximum cell displacement of 1 ($\max(n_x, n_y) = 1$, assuming square-shaped cells). However, for a resolution of 26.6°, a maximum cell displacement of two is required [refer to Fig. 1(b)]. It is possible to reduce the physical track distance by increasing the grid resolution (i.e., making each cell smaller); however, this also increases the computation time due to a larger search space. Thus, the design of $\Gamma_{3\mathrm{D}}$ is dependent on the available computation time, desired track length, and angle resolution for a specific application.

B. Extending the Successor Operator to Four-Dimensional

Consider the extension of $\Gamma_{3\mathrm{D}}$ to four dimensions where each cell has dimensions $(\delta x, \delta y, \delta z, \delta t)$; δt specifies a duration of the time spent inside a 3-D cell. The vector neighborhood concept can be extended to the time dimension such that s' lies at a discretized time level s'_{t_l} that is displaced from s_{t_l} by n_{t_l} time levels; n_{t_l} corresponds to the track traversal time.

The cost of the traversal of a particular track (needed in many search algorithms [1]) in the vehicle motion planning is dependent on the track velocity. Due to the presence of wind, it is not possible to predefine a set cruise velocity for each successor in the 4-D successor operator Γ. However, given a 3-D successor with displacement (n_x, n_y, n_z), it is possible to generate multiple 4-D successors s' with displacement (n_x, n_y, n_z, n_{t_l}) where $n_{t_l} \in N_{t_l}$. The choice of successor time level displacements N_{t_l} is application specific as it is dependent on track lengths, knowledge of expected wind magnitudes, and the minimum and maximum cruise velocities of the vehicle. For a given $\Gamma_{3\mathrm{D}}$, the minimum and maximum cruise velocities can be used to determine an initial estimate of the lower and upper bounds, respectively, for N_{t_l} using (6) (assuming zero wind).

Further refinement of N_{t_l} can be achieved through Monte Carlo simulation over the expected wind conditions by inspecting the resultant cruise and track velocities for a given choice of N_{t_l}.

Note that, for each successor, the cell sequence generated using (2) can be extended to 4-D by simply calculating the time level displacement $n_{t_l}^s$ for each cell s on the sequence

$$\begin{cases} n_{t_l}^s = n_{t_l}\frac{n_x^s}{n_x} & \text{if } |n_x| \geq |n_y|, |n_x| \geq |n_z| \\ n_{t_l}^s = n_{t_l}\frac{n_y^s}{n_y} & \text{if } |n_x| < |n_y|, |n_y| \geq |n_z| \\ n_{t_l}^s = n_{t_l}\frac{n_z^s}{n_z} & \text{otherwise} \end{cases} \tag{5}$$

where n^s is the displacement of cell s from the source node. Note that, in (5), the spatial dimension with the maximum displacement is used to calculate the cell sequence quantized time level displacements, as this gives the maximum sampling resolution.

Given n_{t_l}, the vehicle cruise velocity can be derived from the track length via the track velocity $\vec{v_t}$

$$|\vec{v_t}| = \frac{\sqrt{(s'_x - s_x)^2 + (s'_y - s_y)^2 + (s'_z - s_z)^2}}{n_{t_l}\delta_t}. \tag{6}$$

This track velocity is itself a sum of the cruise and wind velocity vectors

$$|\vec{v_t}|\cos\phi\begin{pmatrix}\sin\theta\\ \cos\theta\end{pmatrix} = |\vec{v_c}|\cos\phi\begin{pmatrix}\sin\alpha\\ \cos\alpha\end{pmatrix} + \begin{pmatrix}v_{w_x}\\ v_{w_y}\end{pmatrix} \tag{7}$$

where θ and ϕ are the horizontal and vertical track angles, respectively, $\vec{v_c}$ is the cruise velocity (e.g., the airspeed of an aircraft), $\vec{v_t}$ the track velocity (e.g., the ground speed of the aircraft), α is the vehicle heading angle, and (v_{w_x}, v_{w_y}) is the horizontal wind magnitude. All angles are measured from the true north in navigational tasks [38]. Note that (7) is formulated in two dimensions instead of three as the horizontal component of the track and track velocity is far greater than the vertical for both UAVs [38] and AUVs [14]. The vertical component of $\vec{v_c}$ and the wind are treated as constraints instead. By separating the x and y components from (7) and then solving the resultant simultaneous equations, it is possible to get an expression for $\vec{v_c}$ given $|\vec{v_t}|$ and (v_{w_x}, v_{w_y})

$$|\vec{v_c}| = \sqrt{|\vec{v_t}|^2 - 2|\vec{v_t}|(v_{w_y}\cos\theta + v_{w_x}\sin\theta) + v_{w_x}^2 + v_{w_y}^2}. \tag{8}$$

Note that we are not interested in the negative root which corresponds to the traversal in the opposite direction.

The preceding section describes in effect a formulation of a vector neighborhood (obtained using a successor operator) like the one in [12] but for (x, y, z, t). Unlike [12], the ensuing sections describe a multistep variant of A* [6] (see Section III-C) that enables the use of a variable successor operator Γ_s for each node s. This variable operator enables the implementation of a multiresolution search and also enables the imposition of a structure on the search space. These are further discussed in Section IV.

C. Search Algorithm

The pseudocode of the MSA* algorithm is listed in Fig. 2. Note that s_0 and s_g refer to the start and goal nodes, respectively. Like A*, the nodes are placed on a priority queue sorted according to the evaluation function f which is itself the sum of the cost to come g and the estimated cost to go $\hat{h}$. In Fig. 2, $Queue.Insert$ refers to the addition of a node s' to the queue such that $f(s^*) \leq f(s)\ \forall\, s \in Queue$, where s^* is the topmost element in $Queue$. $Queue.Pop$ is the removal of this topmost element.

```
1: for all $s \in S$ do
2:     $g(s) \leftarrow \infty$
3: end for
4: $Queue \leftarrow \emptyset$
5: $s \leftarrow s_0$
6: $Queue.Insert(s)$
7: $g(s) \leftarrow 0$
8: while $s \neq s_g$ do
9:     $s = Queue.Pop()$
10:    if $s = s_g$ then return
11:    end if
12:    $S' \leftarrow Succ(\Gamma_s(s))$
13:    for all $s' \in S'$ do
14:        $\hat{g}(s') = g(s) + c(s' \| \gamma_{s'})$
15:        $\hat{f}(s') = g(s') + \hat{h}(s', s_g)$
16:        if $\hat{g}(s') < g(s')$ then
17:            $g(s') \leftarrow \hat{g}(s')$
18:            $Queue.Insert(s')$
19:        end if
20:    end for
21: end while
```

Fig. 2. MSA* pseudocode. Note that at line 12, $Succ(\Gamma_s(s))$ extracts the set of successor nodes $s' \in S'$ where s' is the last cell in each cell sequence $\gamma_{s'} \in \Gamma_s(s)$.

The key distinction between MSA* and A* lies in the cost function c. A* computes the cost (a scalar value) as a function of the cells s and s', whereas the MSA* cost is a function of multiple cells, as defined in the cell sequence [see (1)]

$$g(s') = g(s) + c(s' = s_{j+m-1} \| s = s_j, \ldots, s_{j+m-2}). \tag{9}$$

The cost c is calculated using a two-step process. First, the decision variables x_i (e.g., fuel and risk) are uniquely mapped or calculated from the cell sequence such that $x_i = \rho_i(s, \ldots, s')$ where ρ_i is the mapping function. For example, the total risk probability is the sum of the risk probability density value for each cell on the cell sequence. Note that the constraints can be imposed by setting $c = \infty$ if a particular decision variable exceeds a specified limit (e.g., maximum risk). Otherwise, a multicriteria decision making (MCDM) cost function is used to transform the decision variables into a single cost term c where c is nonzero and monotonic (i.e., $c > 0$). This second step could be a weighted sum aggregation (like that used in [27]–[30]) or a fuzzy mapping (e.g., [31]). Using a weighted sum approach, each decision variable is mapped onto a commensurate scale on the interval [0, 1] using a value function $u_i(x_i)$. The final cost is $c = w_0u_0(x_0) + \cdots + w_{n-1}u_{n-1}(x_{n-1}) + \delta_c$ where n is the number of decision criteria and δ_c is a small positive value to ensure $c > 0$. A comprehensive evaluation of the decision objectives and decision variables for the UAV flight planning is provided in [39] (refer to Section V-A for a brief summary).

D. Cost Optimality of MSA*

It can be shown that MSA* will find the least cost path given a predefined set of successor operators Γ_s for each node $s \in S$

and an MCDM cost function c. As MSA* is derived from A* [6], the cost optimality can be shown in a similar manner as well.

Lemma 1: Consider any globally optimal path $P^* = (s_0, \ldots, s_n)$. It can be shown that P^* is itself composed of optimal paths.

Proof: The optimal path for a given node s_{i_k} is a path $P^* = (s_0, \ldots, s_{i_k})$ such that, for all possible paths $P \in \Pi$, $g(s_{i_k} \| P^*) < g(s_{i_k} \| P)$. Recall that any path is made up of an integer number of trajectory segments K and that each segment is represented by a cell sequence of length m_j for segment j. Thus, the index to a node (or cell) in P^* at the kth trajectory segment is

$$i_k = -k + \sum_{j=0}^{k-1} m_j. \tag{10}$$

For the case where $k = K$, the lemma is trivially true by definition of $P^*_{i_K}$ as $i_K = n$, $P^*_n = (s_0, \ldots, s_n)$. Consider the case for $k = K - 1$ trajectory segments, whose cell sequence $P_{i_{K-1}} = (s_0, s_1, \ldots, s_{i_{K-1}})$ is a subset of the optimal path P^*. If $P_{i_{K-1}}$ is not a least cost path, then there exists another path $P'_{i_{K-1}} = s_0, s'_1, \ldots, s'_{i_{K-2}}, s_{i_{K-1}}$ such that $g(P'_{i_{K-1}}) < g(P_{i_{K-1}})$. However, as the $(K-1)$th cell sequence $s_{i_{K-1}}, \ldots, s_{i_K}$ is unchanged, then, given (9), the cost term c is unchanged. This implies that there exists a path $P'_{i_K} = (s_0, s'_1, \ldots, s'_{i_{K-2}}, s_{i_{K-1}}, \ldots, s_{i_K})$ such that $g(P_{i_K}) < g(P^*_{i_K})$, contradicting the definition of $P^*_{i_K}$. Therefore, $P_{i_{K-1}}$ must also be an optimal path. By mathematical induction, any optimal path P^* must itself be composed of optimal paths. ■

Theorem 1: If the heuristic is admissible [6], then MSA* will find the optimal path if one exists. An admissible heuristic $\hat{h}$ is an estimate of the cost to go that is always less than the actual cost to go, $\hat{h}(s_j, s_{\mathrm{g}}) \leq h(s_j, s_{\mathrm{g}})$.

Proof: Consider an optimal path $P^* = (s_0, \ldots, s_{\mathrm{g}})$ which contains K trajectory segments. On an optimal path, $g(s_j) = g^*(s_j)$ for all $j = (0, 1, \ldots, i_K)$. From line 15, because $\hat{h}(s_j, s_{\mathrm{g}}) \leq h(s_j, s_{\mathrm{g}})$, therefore, $f(s_j) \leq f^*(s_j)$.

In the trivial case where $K = 0$ (i.e., $s_0 = s_{\mathrm{g}}$), MSA* discovers the solution in one iteration. During the initialization (lines 1–7 in Fig. 2), s_0 is placed on the queue with cost $g(s_0) = g^*(s_0) = 0$. Upon the expansion of s_0, MSA* terminates.

Consider the case where $K = 1$, i.e., $s_{\mathrm{g}} \in S'_0$ where $S'_0 = \Gamma_{s_0}(s_0)$. Let S^* denote the set of nodes on the queue that lie on an optimal path. After one iteration (i.e., the expansion of s_0), at least one of the successors s'_0 is a member of S^*. Consider the contrary where none of the nodes $s'_0 \in S'_0$ lie on an optimal path and/or are not on the queue. There are two possibilities, one is that none of the successors are reachable (in which case, no path exists) or at least one of them lies on a least cost path. Note that, if a path exists, then an optimal path also exists.

For this latter case, given a node s'_0, an optimal path $(s_0, \ldots, s'_0)$ that does not contain any nodes in S'_0 must exist because, by Lemma 1, an optimal path $(s_0, \ldots, s_n)$ comprises optimal paths $(s_0, \ldots, s_{n-1}), (s_0, \ldots, s_{n-2}), \ldots$ and none of the nodes in S'_0 lie on an optimal path (by assumption). This is not possible; hence, at least one node s'_0 must lie on an optimal path in which case, by line 16, s'_0 would be added to the queue at the expansion of s_0. Therefore, where a path exists, $S^* \neq \emptyset$ and $s_{\mathrm{g}} \in S^*_0$ for the scenario $K = 1$.

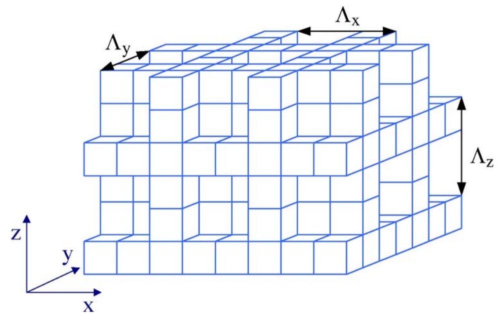

Fig. 3. General lattice structure with (x, y, z) dimensions shown.

The preceding argument can be extended to show that, up until the algorithm termination, $S^* \neq \emptyset$. Let S'_k denote the set of nodes generated by $\Gamma_{s_{i_{k-1}} \in S'_{k-1}}(\Gamma_{s_{i_{k-2}} \in S'_{k-2}}(\ldots \Gamma_{s_0}(s_0)))$—i.e., *all* nodes that can be reached in k trajectory segments. From the previous discussions, all nodes $s : s \in S^*$, $s \in S_k$ $(k = 1)$ are placed on the queue after the first iteration. If the optimal paths of length $k+1$ exist, the expansion of $s : s \in S^*$, $s \in S_k$ must yield nodes $s' : s' \in S^*$, $s' \in S_{k+1}$. Otherwise, as before, there would exist nodes $s' \notin S_k$ that result in the optimal paths of length $k+1$ trajectory segments which is not possible. Hence, $S^* \neq \emptyset$.

Because Γ_s is a finite set for all $s \in S$ and because the trajectory segments incur a nonzero and nonnegative cost c, there are only a finite number of nodes such that $f(s) \leq f^*(s_{\mathrm{g}}) = f^*(s_0)$. Therefore, as $S^* \neq \emptyset$, the nodes on the optimal path $P^* = (s_0, s_{i_1}, \ldots, s_{i_k} = s_{\mathrm{g}})$ are expanded (in sequence) in a finite number of iterations, terminating with the expansion of s_{g}.

It is not possible to terminate without finding the optimal path if one exists. Consider the scenario where MSA* terminates such that $f(s_{\mathrm{g}}) = g(s_{\mathrm{g}}) > f^*(s_0)$. However, by the aforementioned analysis, there exists a node $s \in S^*$ just before the termination such that $f(s) \leq f^*(s_0) < f(s_{\mathrm{g}})$. Hence, s would be expanded instead of s_{g}, contradicting the assumption that MSA* would have terminated. Therefore, MSA* will find an optimal path $(s_0, \ldots, s_{\mathrm{g}})$ in a finite time where such a path exists. ■

IV. Multiresolution Lattice Structure

A class of variable successor operators that can be used to implement a lattice-based multiresolution search space for the purposes of reducing the computation time is presented. The use of variable successor operators Γ_s is made possible by the MSA* search algorithm. As before, the 3-D lattice structure is presented first, followed by a conceptual extension to 4-D. It is shown that lattice-based MSA* reduces the size of the search space without sacrificing the track-angle resolution or soundness [40].

A. Three-Dimensional Lattice

A 3-D illustration of the lattice structure is presented in Fig. 3 with a 2-D cutaway (x–y) view showing the source-successor trajectory segments in Fig. 4. The lattice comprises a series of planes parallel to the x–y, y–z, and x–z Cartesian planes at

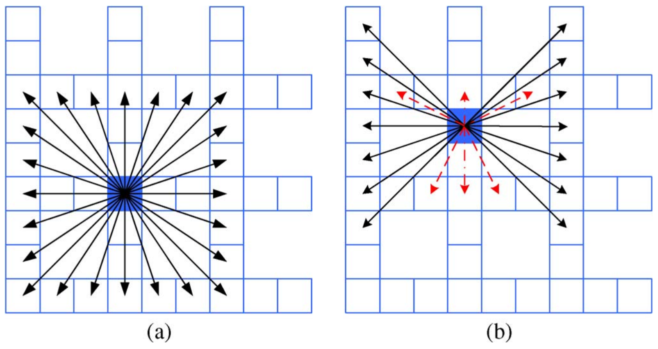

Fig. 4. Top (x–y) view of lattice showing trajectory segments for lattice positions (a) (0, 0) and (b) (0, 2).

regular intervals of Λ_x, Λ_y, and Λ_z (defined in terms of the number of cells) in the x, y, and z planes, respectively.

The lattice design methodology is a three-step process. First, a series of base 3-D successor operators Γ_0 is chosen, one for each search space resolution. The choice of Γ_0 takes into account the required track-angle resolution and track length, both of which are related to the sampling density. Γ_0 must be such so that, in any plane x–y, x–z, or y–z, all the successors lie on the border of a rectangle centered at the source node [as shown in Fig. 4(a)].

Using Γ_0, it is then possible to define the spacing between the planes in the lattice Λ_x, Λ_y, and Λ_z using

$$\begin{aligned}\Lambda_x &= \sup_{\gamma_{n_x}}\{\gamma \in \Gamma_0 : \gamma_{n_x} \geq \gamma_{n_y}, \gamma_{n_z}\}\\ \Lambda_y &= \sup_{\gamma_{n_y}}\{\gamma \in \Gamma_0 : \gamma_{n_y} \geq \gamma_{n_x}, \gamma_{n_z}\}\\ \Lambda_z &= \sup_{\gamma_{n_z}}\{\gamma \in \Gamma_0 : \gamma_{n_z} \geq \gamma_{n_x}, \gamma_{n_y}\} \qquad (11)\end{aligned}$$

where sup denotes the supremum operator (least upper bound). Note that if the start or goal nodes do not lie on the lattice, it is a simple matter to connect those nodes to the one that is on the lattice using a local search technique (refer to [1]).

Using this lattice structure, it is then possible to define individual Γ_s operators for each node on the lattice. This is shown for a 2-D lattice for the sake of clarity in Fig. 4. Due to the regularity of the lattice, the nodes located at equivalent positions on the lattice share the same successor operator $\Gamma_{\vec{p}}$ for position $\vec{p}$. Two positions are equivalent if and only if they are separated by the integer multiples of Λ_x, Λ_y, and Λ_z cells. A lattice position $\vec{p}$ can be uniquely defined based on the modulus

$$\vec{p} = (\mathrm{mod}(x, \Lambda_x), \mathrm{mod}(y, \Lambda_y), \mathrm{mod}(z, \Lambda_z)). \qquad (12)$$

Referring to Fig. 3, the total number of unique lattice positions n_p is

$$n_p = \Lambda_x\Lambda_y + \Lambda_x(\Lambda_z - 1) + (\Lambda_y - 1)(\Lambda_z - 1). \qquad (13)$$

Consider the case where the source node is at lattice position (0, 0, 0), i.e., at the intersection of the lattice planes [see Fig. 4(a)]. The trajectory segments are chosen to terminate at the successors that lie on the border of a rectangle centered on the source node with dimensions of $(2\Lambda_x, 2\Lambda_y, 2\Lambda_z)$ cells. Therefore, $\Gamma_{\vec{p}=(0,0,0)} = \Gamma_0$. For the cells located at different positions on the lattice [refer to Fig. 4(b)], the successors are chosen to maximize the number of identical successors

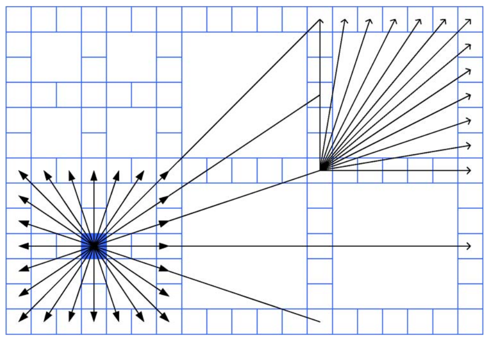

Fig. 5. Multiresolution lattice with $\Lambda_x = \Lambda_y = 3$ on the left and $\Lambda_x = \Lambda_y = 6$ on the right. Selected trajectory segments are shown for the sake of clarity.

to $\Gamma_{(0,0,0)}$. Additionally, where possible, the successors are chosen to terminate at lattice position (0, 0, 0). This ensures that the same track angle can be maintained over consecutive trajectory segments to avert unnecessary turns.

B. Three-Dimensional Multiresolution Lattice

The purpose of multiresolution sampling is to reduce the total number of nodes and thus reduce the computation time. In many applications, it is possible to divide the search space into regions of fine sampling resolution and regions of coarse sampling resolution. In the UAV flight planning, for example, a fine sampling resolution is required at lower altitudes, but a coarse sampling resolution can be used for high-altitude en route airspace. It is easy to implement the multiresolution search by using multiple base successor operators Γ_0^i.

Consider the division of the search space into a series of N rectangular-prism-shaped regions, each of which has a lattice resolution of $(\Lambda_x^i, \Lambda_y^i, \Lambda_z^i)$, $i = 1, 2, \ldots, N$ and a base successor operator Γ_0^i. Note that N is typically a small number as it is necessary to check the bounds of each region at every iteration. Each region must have dimensions that are a multiple of Λ_x^i, Λ_y^i, and Λ_z^i. This ensures that all the trajectories must terminate on and originate from a lattice plane separating the two regions (refer to Fig. 5).

Furthermore, assume that, for any two adjacent regions i and j, Λ_x^i, Λ_y^i, and Λ_z^i are integer multiples of Λ_x^j, Λ_y^j, and Λ_z^j, respectively. This way, the successors in Γ_0^i are displaced at the integer multiples of those in Γ_0^j, which ensures that all horizontal track angles [calculated using (3)] in region j also exist in region i (see Fig. 5). Unfortunately, this is not the case for the vertical track angle even though the angles in the x–z and y–z planes are replicated in region i. To avoid a large increase in the number of successors, it is also possible to filter out the successors in Γ_0^i that are on the track angles not represented in Γ_0^j.

The aforementioned multiresolution lattice provides a means for the fine and coarse sampling corresponding to smaller and larger values of Λ, respectively. There is no reduction in the track-angle resolution for the coarsely sampled regions as larger values of Λ enable higher track-angle resolutions. Additionally, each track is evaluated at the cell resolution using the cell sequences defined in Section III-A. This guarantees the path soundness [40, Ch. 25.6] by avoiding the problem of mixed cells (which contains free space and obstacles [1]).

C. Four-Dimensional Multiresolution Lattice

The extension of the previous 3-D lattice to four dimensions involves the selection of a suitable set of values $n_{t_l} \in N_{t_l}$ for each 3-D successor in $\Gamma_{\vec{p}}$ using the methodology described in Section III-B. The full 4-D multiresolution lattice structure is implicitly defined through the variable successor operators where, at each iteration of the MSA* search, $\Gamma_{\vec{p}}$ is selected based on (12) and the boundaries of each Γ_0^i region. This approach enables consistent track-angle resolution across the fine- and coarse-resolution regions without sacrificing the soundness.

In addition, the lattice structure reduces the memory usage. The underlying cell grid of MSA* contains $N_x N_y N_z N_{t_l}$ nodes where N_x, N_y, N_z, and N_{t_l} are the total number of sample points in the x, y, z, and t dimensions, respectively. The total memory requirement (i.e., number of nodes) N for a lattice can easily be derived by counting the number of nodes in the x, y, and z planes (refer to Fig. 3) and then subtracting the overlap regions

$$N = N_{t_l}(N_y N_z \alpha_x + N_x N_z \alpha_y + N_x N_y \alpha_z - \alpha_x \alpha_y N_z - \alpha_x \alpha_z N_y - \alpha_y \alpha_z N_x + \alpha_x \alpha_y \alpha_z) \quad (14)$$

where $\alpha_x = \lfloor (N_x - 1/\Lambda_x) + 1 \rfloor$ (and, similarly, for y and z) and all division operations are the integer divisions. Note that the $N_y N_z \alpha_x$ term in (14) counts the number of nodes in the x plane for all x planes, where α_x is the number of x planes (similarly, for y and z). The term $-\alpha_x \alpha_y N_z$ subtracts the overlaps between the x and y planes (similarly, for the overlaps between the x and z planes, and y and z planes), and $\alpha_x \alpha_y \alpha_z$ represents the overlap between the $\alpha_x \alpha_y N_z$, $\alpha_x \alpha_z N_y$, and $\alpha_y \alpha_z N_x$ terms.

V. Experimental Analysis

This section discusses some of the practical aspects of implementing the proposed algorithm, including the evaluation of MSA* against an existing vector neighbor-based search algorithm (like [12]) in the simulation. Such a comparison is used to evaluate the computational efficiency of MSA*.

A. UAV Flight Planning Application

The UAV mission flight planning problem was chosen to provide a practical context for the evaluation of MSA*. This is an important application as onboard mission flight planning (particularly the online replanning) has been shown to be a key enabler in the operation of UAVs in the National Airspace System [39]. The mission being undertaken is the delivery of a medical package to a remote location using a small UAV. This mission is operated under visual flight rules using Australian Civil Aviation Regulations [41]. The medical delivery task is ideal for evaluating a 4-D search algorithm due to the presence of multiple decision criteria, dynamic elements in the operating environment, and the significant effect of wind on a small UAV. The three major decision objectives for the medical package delivery mission are safety, the rules of the air, and mission efficiency [39].

The safety objective is modeled with the aircraft separation management, storm cell avoidance, and population risk criteria. For simulation purposes, the aircraft separation requirement (5-nmi horizontal and 1000-ft vertical) for en route airspace is adopted. The cylindrical-shaped separation region is represented with an approximate probabilistic model [39]. This model is similarly used to describe storm cells. Finally, the population risk criterion refers to the minimization of the risk presented to people and property on the ground in the event of a crash. For the purposes of simulation, this risk value is approximated with a normalized population density (NPD) value.

The flight plan must also conform to the rules of the air, such as the cruising level rule, low flying restrictions (minimum altitude above ground level), and segregated airspace (avoiding no-fly zones). For aircraft flying on headings from 0° to 179°, the permissible flight levels are at odd multiples of 1000 ft plus 500 ft above mean sea level (AMSL) (e.g., 1500, 3500, and 5500 ft AMSL). For headings between 180° and 359°, the cruise levels are at even multiples of 1000 ft AMSL plus 500 ft (e.g., 2500, 4500, and 6500 ft AMSL). The cruising level rule is intended to minimize the risk of a head-on collision and is mandatory above 5000 ft.

The flight plan also needs to optimize for the objectives of the mission itself (i.e., the delivery task). These objectives include the delivery time (i.e., the time of arrival at the goal node) and fuel consumption. With a 4-D search, it is possible not only to find a path that minimizes the delivery time but also to designate a specific delivery time or acceptable time window (like with [16]). The flight time, along with the cruise velocity, altitude, and rate of climb, is the parameter used to optimize the fuel consumption.

These decision variables, in combination with the dynamic constraints of the aircraft, are used to calculate the cost term c in (9). Note that, for the purposes of planning, it is assumed that all situational awareness information (e.g., wind information and information about other aircraft) is available. For further details and candidate data sources for each decision variable, refer to [39]. Note that, as the dynamic constraints are closely linked with the chosen successor trajectory segments in Γ, these are discussed together in the following section.

B. Experimental Setup

The primary purpose of this experimental analysis is to compare the computational efficiency and solution path of the proposed algorithm with that of existing algorithms. In these comparisons, each test algorithm uses a different (set of) successor operator(s) but the same cost function c (a weighted sum of the utility values) and heuristic function h.

1) Test Algorithms: Two different variants of MSA* are compared against a benchmark algorithm, Vector A*, on 1000 randomly generated planning scenarios. Vector A* is a direct extension of A* using a vector neighborhood (like that used in [12]). The successor operator is chosen to reflect the base successor operator used in the other test algorithms and is shown in Fig. 6. Using this successor operator, there are 360 successors for each source node. Vector A* is in effect a special case of MSA* where Γ_s is constant throughout the entire search space. Due to the popularity of A* and related algorithms in robotics [42], Vector A* serves as an ideal benchmark of calculation time and path cost for a deterministic 4-D planning algorithm

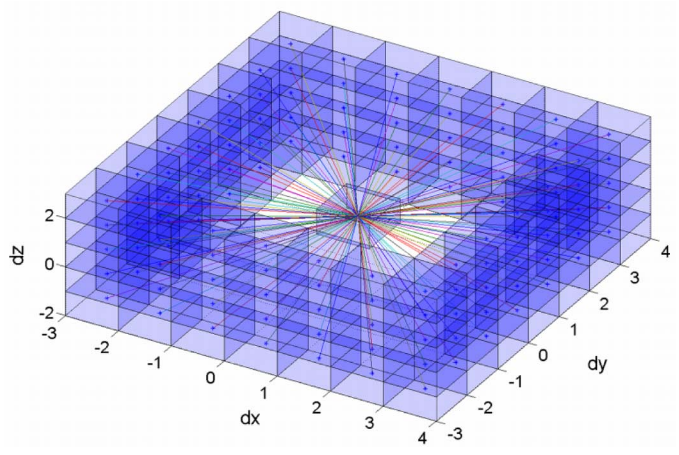

Fig. 6. Chosen Γ_0 successor operator, showing (center) source cell and successor cells joined by trajectory segments. $\Lambda_x = 3$, $\Lambda_y = 3$, $\Lambda_z = -\infty$, and $N_{t_l} = \{2, 3, 4\}$ min. Note that $\Lambda_z = -\infty$ corresponds to a lattice where there are no z-planes.

with selectable track-angle resolution. Two variants of MSA*, MSA*1 and MSA*2, are tested against the benchmark. MSA*1 uses a single fine-resolution lattice based on Γ_0, as shown in Fig. 6. MSA*2, on the other hand, uses a multiresolution lattice where $N = 2$. A fine-resolution lattice (based on Γ_0 in Fig. 6) is used for altitudes below 7000 ft, and a coarse-resolution lattice $(\Lambda_x = 6,\ \Lambda_y = 6,\ \Lambda_z = -\infty,\ \text{and}\ N_{t_l} = \{4, 6, 8\}\,\text{min})$ is used for altitudes above 7000 ft.

All the experiments were performed on a 3.3-GHz Intel Core 2 Duo QX6850 CPU with 4 GB of physical RAM running at 32-b Microsoft Windows XP.

2) Dynamic Constraints: The dynamic constraints of the aircraft were considered in the selection of Γ_0 in Fig. 6. Oftentimes, these dynamic constraints are modeled with a minimum turn radius [1]. Assuming a maximum airspeed of 126 kn, a bank angle of 30°, and a force of 1 g (32.2 ft/s^2), the worst case turn radius is approximately 0.4 nmi (refer to [38, (3.9.10)]). As the turn radius is less than half the cell size, it is possible to execute a 180° turn within the bounds of a single cell. However, it is still desirable to minimize the turn angle as it is difficult for the flight controller to execute such a turn with accuracy under strong wind conditions. The turn angles are further discussed in Section V-C.

For UAV operations, it is also necessary to incorporate climb/descent rate constraints and a maximum airspeed constraint (a constant value). The maximum climb rate, however, decreases with altitude and is zero at the aircraft ceiling [38]. At sea level, the maximum climb rate for a small UAV is limited to approximately 1000 ft/min [43]. This matches the maximum climb rate achieved using Γ_0 under no-wind conditions

$$\frac{\max\limits_{n_z}(n_z\delta_z)}{\min\limits_{n_{t_l}\in N_{t_l}}(n_{t_l}\delta_t)} = 1000\ \text{ft/min}. \tag{15}$$

3) Simulation World: The simulation worlds were generated randomly to enable a Monte Carlo evaluation of the test algorithms. Each simulation world comprises a terrain map, no-fly zones, other aircraft, storm cells, wind map, and population density map (as a simple model of risk presented to the people and property on the ground). For each world, a number of start and goal pairs were randomly chosen. The mission area for each world was arbitrarily chosen to be 50 nmi × 50 nmi × 15 000 ft × 90 min with a cell resolution of 1 nmi × 1 nmi × 1000 ft × 1 min (1 nmi = 1852 m and 1 ft = 0.3048 m). Note that the maximum distance of the search area approximately matches the maximum operating range of the RQ-7A Shadow UAV [43].

An artificial terrain map is randomly generated through the summation of bivariate Gaussian functions with randomly chosen parameters (A, b, c, σ, n). The population density is also generated using this equation

$$z(x, y) = \sum_{i=0}^{n} A_i e^{-\frac{(x-b_i)^2+(y-c_i)^2}{\sigma_i^2}}. \tag{16}$$

The maps for the other decision variables can also be randomly generated through a random selection of the parameter values. For example, the parameters for a cylindrical aircraft separation zone are position, velocity, standard deviation, radius, and height. The velocity is assumed to range between 50 kn and a speed limit (for flights below 10 000 ft) of 250 kn [41]. The radius and height are specified in aviation regulations. Similarly, the storm cells are randomly generated with an average radius of 13.5 nmi and a height of 8 nmi [44, Fig. 5]. The rate of movement of a storm cell is assumed to be between 10 and 40 kn for altitudes between 0 and 15 000 ft [44, Fig. 1]. A method for modeling each of the remaining decision variables is provided in [39].

Finally, a simple algorithm was used to generate wind maps that mimic the real-world winds. First, a number of seed nodes are randomly generated at different positions (x, y); each seed is characterized by a position $\vec{p_i}$, a direction ϕ_i, and a vector of wind magnitudes $\vec{m}_z$ for each altitude level z. For each node $s = (x, y, z)$ in the world space, a weighting vector $\vec{u}$ is calculated

$$u_i = a_0|\vec{d_i}| + a_1|\angle\vec{d_i} - \phi_i| \tag{17}$$

where $\vec{d_i} = \vec{s} - \vec{p_i}$ and a_0 and a_1 are the weights. The largest element in $\vec{u}$ is then scaled by a^*; this gives the "winning seed" more weighting. For a given node s, the wind magnitude is $f_m(s) = \vec{u} \cdot \vec{m}_z$. The wind magnitude for each altitude level is randomly chosen based on the average wind speeds (refer to [39]). The direction f_d is calculated in a similar manner, $f_d(s) = \vec{u} \cdot \vec{\phi} + \sigma_z$ where σ_z is a small random perturbation added to simulate the wind shear.

C. Results

A Monte Carlo simulation of the three test algorithms is performed on 1000 randomly generated planning scenarios. The results of these simulations are presented hereinafter and evaluated with respect to computation time and path cost. In addition, the algorithms are also evaluated on three special case test scenarios. These were constructed to determine the effect of local minima and to test the adaptability of the planner to situations where the vertical wind velocity exceeds the aircraft performance.

An illustration of a typical multi-objective planning scenario is provided in Figs. 7 (showing other aircraft and no-fly zones) and 8 (risk map). The solution paths using Vector A*, MSA*1,

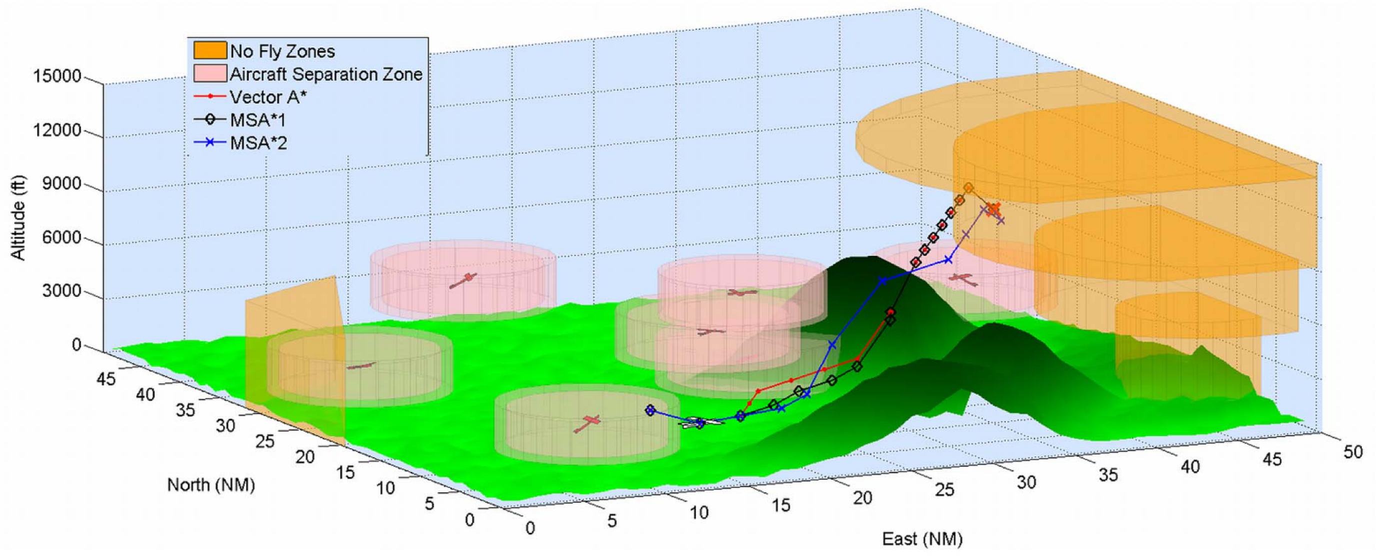

Fig. 7. Example planning scenario showing no-fly zones and other aircraft at $t = 120$ s. Note that, for the aircraft and weather, the inner cylinder represents the separation zone/storm cell extents (around the expected position) and the outer cylinder is the 2σ uncertainty boundary (which grows with time). Note also that the red X marks the goal position.

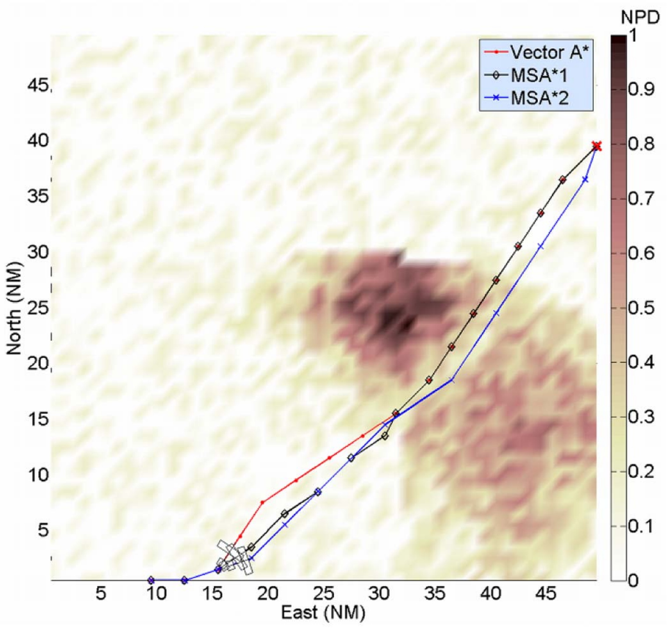

Fig. 8. Example planning scenario risk represented by an NPD map.

TABLE I
COMPUTATION TIME AND LOOP COUNT

	μ_t	σ_t	min	max	μ_n	σ_n
MSA*2	4.46s	2.36s	0.31s	16.6s	65501	34250
MSA*1	9.23s	4.93s	0.53s	35.2s	161571	88386
Vector A*	19.25s	10.41s	0.81s	77.9s	289015	160575

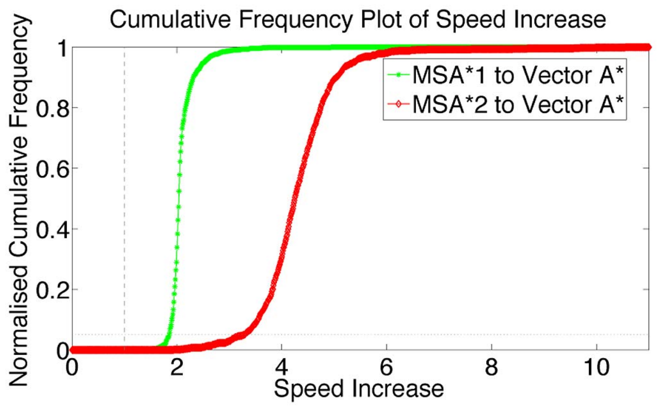

Fig. 9. Normalized frequency histogram of speed increase of MSA*1 and MSA*2 to Vector A*.

and MSA*2 are also shown on each of these figures. In Fig. 7, all three planners select a path that avoids an aircraft on a converging course by descending and heading in an easterly direction. Once a risk of collision is averted, the paths continue in a shortest path fashion toward the goal (marked by a red cross). There are deviations only to avoid terrain (where the paths hop over a mountain in Fig. 7) and to route around high-risk (population density) areas (see Fig. 8). Note that, as shown in Section III-D, each algorithm finds a path that satisfies all the given constraints while minimizing the overall path cost (which is a multi-objective cost function).

1) Computation Time: The mean and the standard deviation for the computation time (μ_t and σ_t, respectively), along with the minimum and maximum computation times, and the loop count (μ_n and σ_n, respectively) are presented in Table I for each test algorithm. From the results, it can be deduced that a lattice-based successor operator can significantly reduce the total computation time and that further time savings can be achieved with a multiresolution lattice. A cumulative histogram of the speed increase is provided in Fig. 9 along with a statistical summary of the speed increase in Table II. For the test resolution level, Vector A*, MSA*1, and MSA*2 are all suitable for the onboard replanning as the computation time is well within the minimum track traversal time of 2 min, as specified in N_{t_l}.

TABLE II
SPEED INCREASE OVER VECTOR A*

	Percentile (%)						
	≤0	≤1	≤25	≤50	≤75	≤100	Mean
MSA*1	0.98	1.69	1.98	2.04	2.12	4.94	2.09
MSA*2	1.94	2.52	3.91	4.25	4.66	10.55	4.30

TABLE III
PATH COST RATIO

	μ_c	σ_c
MSA*1 to Vector A*	0.9891	0.0307
MSA*2 to Vector A*	1.0334	0.0376

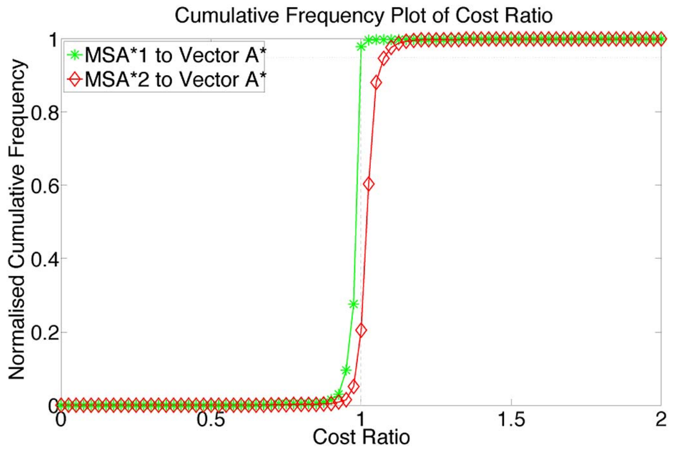

Fig. 10. Cumulative histogram of relative path cost.

2) *Total Path Cost:* The mean μ_c and the standard deviation σ_c in the ratio of the path cost between MSA*1, MSA*2, and Vector A* are presented in Table III. A cumulative histogram of the ratios is illustrated in Fig. 10. As the successor operator $\Gamma_{\vec{p}}$ in MSA*1 is largely similar to Γ in Vector A*, it is not surprising to find that both return paths are of approximately equivalent cost. On a particular note, however, is the fact that, on average, MSA*2 finds paths that are only 3.3% costlier than Vector A*. Therefore, it can be seen that MSA* finds paths of equivalent cost but with significantly less computation time.

It is observed that each of the three test algorithms returns a solution path that tends to follow the profile of a straight line (shortest path). This is attributable to the minimization process of A* and the fact that all trajectory segments have a nonzero and nonnegative cost value. As a result, the turn angles are typically small even without the explicit optimization of turn angles. The mean turn angles (and standard deviations) for Vector A*, MSA*1, and MSA*2 are 11.7° (19.0°), 12.7° (22.4°), and 16.4° (21.9°), respectively.

D. Special Cases

It is widely acknowledged that A* and best first search algorithms in general require significantly more computation time in the presence of local minima [1]. This was tested for the single and double bug trap case, as recorded in Table IV; the double bug trap case is illustrated in Fig. 11. It can be seen that, even though the absolute computation time is approximately

TABLE IV
COMPUTATION TIME

	Single Bug Trap		Double Bug Trap	
	Time	Loop Count	Time	Loop Count
MSA*2	9.59s	201197	9.17s	194981
MSA*1	23.45s	515657	22.61s	503871
Vector A*	51.14s	922544	50.65s	926276

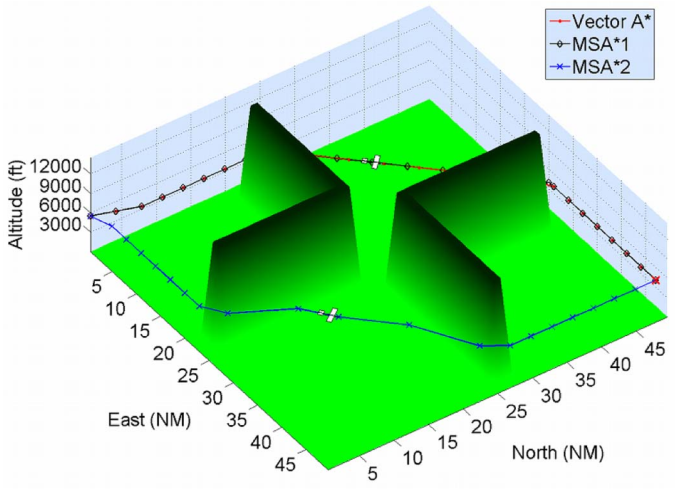

Fig. 11. Double bug trap case.

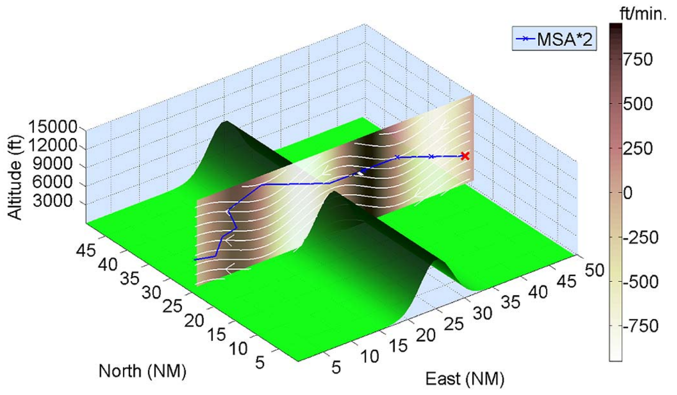

Fig. 12. Mountain wind simulation. Solution is found in 5.14 s.

double to 2.5 times the mean obtained in the previous Monte Carlo simulations, the relative computation time between Vector A*, MSA*1, and MSA*2 remains approximately the same as before.

A simulation scenario which mimics the presence of strong up/downdrafts in mountainous regions (where the vertical wind velocity can exceed the vehicle's climb rate) is depicted in Fig. 12. Even though a variety of wind conditions was simulated in the previous Monte Carlo experiment, this experiment specifically studies the effect of wind by setting other decision variables (e.g., no-fly zones, other aircraft, storm cells, and risk) to zero. As shown in Fig. 12, only MSA*2 successfully finds a traversable path that satisfies the aircraft climb constraints. The chosen path climbs in a switchback pattern before "hopping over" the mountain. Recall that, as the aircraft's maximum climb rate decreases with altitude, it is necessary to climb to 13 500 ft to accommodate the loss of altitude in the downdrafts region. The reason that MSA*2 successfully finds a path while Vector A* and MSA*1 fail is the higher climb and descent rate required by the fine-resolution successor operator. The same vertical distance is covered in a shorter time using the fine-resolution operator (e.g., 1000 ft in 2, 3, or 4 min) compared to the coarse-resolution operator (e.g., 1000 ft in 4, 6, or 8 min).

VI. Discussion

This section reviews the proposed algorithm with respect to the existing works in light of the practical simulation results and theoretical findings.

A. Online Replanning

The primary objective of the simulation experiments presented in Section V is to determine whether the algorithm is fast enough for the online replanning. The online replanning is needed to mitigate the uncertainty and unpredictably of an outdoor operating environment. Consider the practical implementation of a planner (such as MSA*) on a UAV. A replan is triggered when the environment changes or when the vehicle deviates beyond the tolerance bounds on the originally planned path. It is assumed that a predictor module provides the planner (e.g., MSA*) with a start node such that the time required to reach the start node (from the current state) is a conservative estimate of the planning time. Thus, the planner completes the planning (while the UAV is flying under reactive local control) prior to reaching the predicted start node—if this is not the case, the process is repeated. In practice, if the planning time is short relative to the dynamics of the mission (i.e., any changes to the predicted operating environment are within the tolerance bounds during the planning), this would not introduce instability into the overall control and planning loop.

An indicator of the available planning time can be derived from the minimum track traversal time as the motion plan is made up of discrete trajectory segments (i.e., tracks). For the successor operator selected in Fig. 6, the mean planning times for MSA*2, MSA*1, and Vector A* (4.46, 9.23, and 19.25 s, respectively) were found to be much smaller than the minimum track traversal time (2 min). All three test algorithms were also shown to be capable of finding a path within the time constraints of the online replanning for environments containing deep local minima and narrow escape passages (as per Fig. 11).

In these experiments, it was found that the proposed algorithm offered an approximately twofold reduction in the computation time. Further reductions were obtained by using a multiresolution lattice. This increased speed is significant when planning over a larger search space or on a more difficult search space. For a 100 nmi $\times$ 100 nmi $\times$ 15 000 ft $\times$ 180 min search space, a similar Monte Carlo experiment found that MSA*2 is still able to meet the requirements for the online replanning with a mean planning time of 48.25 s and a standard deviation of 20.62 s (which is less than the minimum track traversal time of 2 min). However, Vector A* does not meet the requirements as it takes approximately four times the computation time. Similarly, when presented with local minima, which are known to be difficult to solve for best first search algorithms like A*, the computational efficiency of MSA* over Vector A* is significant in meeting the online replanning constraints [1].

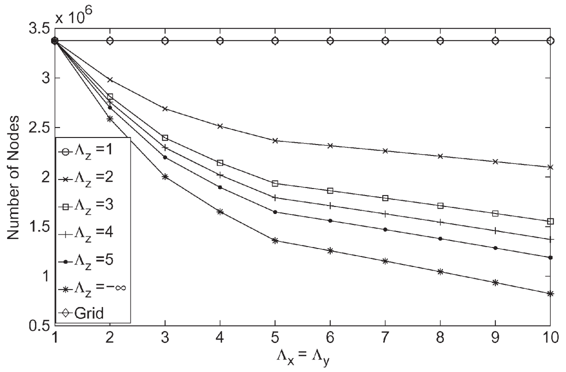

Fig. 13. Number of nodes in the search space for different values of Λ. Note that $\Lambda_z = -\infty$ corresponds to the constrained vertical-track-angle case described in Section IV-A.

The previous discussion of the algorithm computation time assumes that, in each case, we plan from scratch. This approach of always discarding previous planning information was adopted because, in applications such as a UAV package delivery, online changes can occur anywhere in the search map and affect large swaths of the search space. If a large number of nodes are changed and/or changes occur close to the goal node, replanning algorithms like D* and D* Lite are *less* efficient than one that plans from scratch [42]. The presence of a fast moving aircraft and storm cells, for example, can affect large areas of the search space that are not necessarily localized around the vehicle's current position. Hence, it is more efficient to plan from scratch each time.

Due to the time critical nature of the online replanning, it is preferable to use a fast and near-optimal planner rather than an optimal planner which may be too slow. Under these conditions, MSA*2 is the best candidate for the online replanning out of the three test algorithms.

B. Lattice Structure

The computational efficiency of MSA* compared to Vector A* can be attributed to a smaller lattice-structure-based search space compared to a full 4-D grid. With the exception of the successor operator and cell sequence based sampling, Vector A* is virtually identical to MSA*. Using (14), a plot of the number of nodes for a search space of dimensions 50 $\times$ 50 $\times$ 15 $\times$ 90 given different values of Λ assuming $\Lambda_x = \Lambda_y$ is shown in Fig. 13. Note that the memory required in a full grid corresponds to the case where $\Lambda_x = 1$, $\Lambda_y = 1$, or $\Lambda_z = 1$.

From Fig. 13, it is evident that larger values of Λ produce a lattice structure with fewer sample nodes. However, the corresponding successor operator Γ_s has potentially more successors per node with greater track-angle resolution and a greater track length. As a result, fewer search iterations are required, but each iteration incurs more computation time. For example, it is possible to evaluate 17 400 nodes/s (on average) using MSA*1, whereas only 14 750 nodes/s is possible (on average) using MSA*2. It can be seen that the variable successor operator Γ_s is a crucial application-specific design parameter that influences the path cost, the traversability of the path, and the computation time. For the demonstration for UAV applications, it has been shown that the selected fine-resolution and, particularly, the multiresolution successor operators are effective at delivering a solution of comparable cost with significant savings in the computation time. The use of a coarse-resolution successor operator Γ_s for high altitudes in MSA*2 is particularly suited to the UAV planning because of the scarcity of obstacles and reduced climb rate at high altitudes (refer to Section V-D).

The lattice structure presented here is similar to the framed quad/octree presented by Yahja *et al.* [9]. A key improvement in terms of 3-D sampling is that the proposed lattice comprises sample planes that are one cell wide (see Fig. 4), whereas that used in framed octree is two cells wide [9, Fig. 4]. This results in fewer nodes in the search space and hence reduced the memory and computation time requirements. Additionally, the track angle in a framed octree is constrained to intervals of 45° when transitioning between quadtree nodes. Finally, the proposed method guarantees the path soundness by sampling each trajectory segment at the same high-resolution cell size, thus avoiding the problem of mixed cells when using cell-decomposition-based methods (such as quad/octree-based methods like [9]).

C. Uncertainty

MSA* returns a path comprising a sequence of cells which form a corridor in 4-D space around the planned trajectory. This differs from the existing vector neighbor-based methods, like [12], which do not explicitly associate cells or a volume of space with each trajectory segment. Such a cell sequence provides an inherent tolerance to uncertainty. This approach avoids the intractability of directly incorporating the uncertainty into the search space (using methods such as Markov decision processes) for a large high-dimensional search space [1].

The level of tolerance can be determined by finding the minimum perpendicular distance d between the track and the cell boundaries for each cell on the trajectory segment. This is shown in Fig. 14 where $\overrightarrow{AB}$ is the trajectory segment and $\overrightarrow{DC}$ is the perpendicular distance to an exterior corner of a cell on the sequence $\gamma_{s'}$. An exterior corner is one that is not completely enclosed by adjacent cells. The angle θ can be determined by the dot product of vector AB and AC

$$\overrightarrow{AB} \cdot \overrightarrow{AC} = |\overrightarrow{AB}||\overrightarrow{AC}| \cos\theta. \tag{18}$$

In $\triangle ADC$, as $\angle ADC = 90°$ (by definition), then $AD = AC \cos\theta$. The position of D can then be determined using a simple vector line equation and AD

$$D = \vec{A} + \frac{\overrightarrow{AB}}{|\overrightarrow{AB}|} |\overrightarrow{AC}| \cos\theta. \tag{19}$$

Because the cell sequence generated using (2) only includes cells that intersect the track, if D does not lie within the cell, then that particular corner is ignored. Otherwise, the perpendicular distance DC is

$$|\overrightarrow{DC}| = |\overrightarrow{AC}| \sin\theta. \tag{20}$$

The value of d is determined by taking the minimum DC value for all corners of all cells in $\gamma_{s'}$. Note that $\theta = 0$ implies that the trajectory intersects a cell edge/corner, in which case all adjacent cells were already included in the cell sequence. Hence, this implies a nonexterior cell corner. For the successor operator depicted in Fig. 6 and a 3-D cell size of 1 nmi × 1 nmi × 1000 ft, the minimum 3-D tolerance is 166 ft, and the minimum horizontal (x–y) tolerance is 0.14 nmi. Note that all transition maneuvers (i.e., turns) needed to transition between tracks are assumed to be of negligible cost compared to the tracks themselves. These maneuvers are assumed to stay well within the boundaries of the cell sequence.

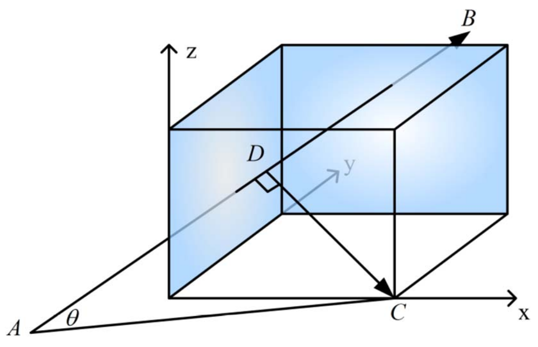

Fig. 14. Illustration of a cell in the cell sequence for a given trajectory segment AB.

It is possible to modify the cell sequence returned by the method described in Section III-A to enforce a minimum tolerance constraint (3-D or horizontal only). For each exterior corner of each cell that does not satisfy the distance constraint, it is a simple matter to include *all* cells adjacent to that corner to increase the minimum tolerance. This procedure is repeated until all exterior corner points satisfy the minimum tolerance. The time level of each added cell can be determined in the same manner as in (5).

VII. Conclusion

This paper has presented MSA*, a method for motion planning using a variable successor operator that finds the least cost paths. A variable successor operator enables the variable track length, angle, and velocity trajectory segments that are modeled using a computer-graphics-inspired cell sequence. This provides an inherent tolerance to uncertainty based on the minimum distance between the track and cell sequence boundaries.

Additionally, a variable successor operator enables the imposition of a multiresolution lattice structure on the search space which drastically reduces the number of search nodes and search time. The extensive simulations for a UAV flight planning task have revealed that multiresolution MSA* is approximately four times faster (on average) than vector neighborhood-based A* (Vector A*) but returns paths of approximately the same cost (an average path cost ratio of 1.033). Even with a uniform fine-resolution lattice, MSA* is still twice as fast as Vector A* with an average path cost ratio of 0.99. It has been shown that MSA* is suited to the online replanning with an average computation time (4.46 s for multiresolution MSA*) that is a fraction of the minimum track traversal time (2 min).

Future work primarily revolves around the implementation and real-world testing of the proposed algorithm in a closed-loop intelligent control system. Such an implementation includes the predictor and scheduling elements discussed in Section VI-A and a study of the stability of the overall system.

Additional avenues for the study include the use of heuristic inflation (such as with anytime replanning A* [42]) and multi-objective heuristics to further reduce the computation time.

Acknowledgment

The authors would like to thank Dr. O. Obst for his insightful feedback on this paper.

References

[1] S. M. LaValle, *Planning Algorithms*. New York: Cambridge Univ. Press, 2006.
[2] C. C. Eriksen, T. J. Osse, R. D. Light, T. Wen, T. W. Lehman, P. L. Sabin, J. W. Ballard, and A. M. Chiodi, "Seaglider: A long-range autonomous underwater vehicle for oceanographic research," *IEEE J. Ocean. Eng.*, vol. 26, no. 4, pp. 424–436, Oct. 2001.
[3] S. S. Wegener, S. S. Schoenung, J. Totah, D. Sullivan, J. Frank, F. Enomoto, C. Frost, and C. Theodore, "UAV autonomous operations for airborne science missions," in *Proc. AIAA 3rd 'Unmanned Unlimited' Tech. Conf., Workshop Exhib.*, Chicago, IL, 2004.
[4] W. B. Powell, *Approximate Dynamic Programming*. Hoboken, NJ: Wiley-Interscience, 2008.
[5] J. S. Mitchell and C. H. Papadimitriou, "Weighted region problem: Finding shortest paths through a weighted planar subdivision," *J. Assoc. Comput. Mach.*, vol. 38, no. 1, pp. 18–73, Jan. 1991.
[6] P. Hart, N. Nilsson, and B. Rafael, "A formal basis for the heuristic determination of minimum cost paths," *IEEE Trans. Syst. Sci. Cybern.*, vol. SSC-4, no. 2, pp. 100–107, Jul. 1968.
[7] D. Ferguson and A. Stentz, "Using interpolation to improve path planning: The field D* algorithm," *J. Field Robot.*, vol. 23, no. 2, pp. 79–101, Feb. 2006.
[8] A. Nash, K. Daniel, S. Koenig, and A. Felner, "Theta*: Any-angle path planning on grids," in *Proc. AAAI Conf. Artif. Intell.*, Jul. 22–26, 2007, pp. 1177–1183.
[9] A. Yahja, S. Singh, and A. Stentz, "An efficient on-line path planner for mobile robots operating in vast environments," *Robot. Auton. Syst.*, vol. 33, no. 2/3, pp. 129–143, 2000.
[10] J. Rubio and S. Kragelund, "The trans-pacific crossing: Long range adaptive path planning for UAVs through variable wind fields," in *Proc. 22nd Digital Avionics Syst. Conf.*, 2003, vol. 2, pp. 8.B.4.1–8.B.4.12.
[11] D.-W. Gu, W. Kamal, and I. Postlethwaite, "A UAV waypoint generator," in *Proc. AIAA 1st Intell. Syst. Tech. Conf.*, Sep. 20–22, 2004, pp. 1–6.
[12] M. Pivtoraiko and A. Kelly, "Generating near minimal spanning control sets for constrained motion planning in discrete state spaces," in *Proc. IEEE/RSJ Int. Conf. Intell. Robots Syst.*, 2005, pp. 3231–3237.
[13] J. Carsten, D. Ferguson, and A. Stentz, "3D field D*: Improved path planning and replanning in three dimensions," in *Proc. IEEE Int. Conf. Intell. Robots Syst.*, 2006, pp. 3381–3386.
[14] C. Petres, Y. Pailhas, P. Patron, Y. Petillot, J. Evans, and D. Lane, "Path planning for autonomous underwater vehicles," *IEEE Trans. Robot.*, vol. 23, no. 2, pp. 331–341, Apr. 2007.
[15] Y. Kim, D.-W. Gu, and I. Postlethwaite, "Real-time path planning with limited information for autonomous unmanned air vehicles," *Automatica*, vol. 44, no. 3, pp. 696–712, Mar. 2008.
[16] P. Tompkins, A. T. Stentz, and W. R. L. Whittaker, "Mission-level path planning for rover exploration," in *Proc. 8th IAS*, Mar. 2004, pp. 529–537.
[17] K. Fujimura, "Path planning with multiple objectives," *IEEE Robot. Autom. Mag.*, vol. 3, no. 1, pp. 33–38, Mar. 1996.
[18] D. Rathbun, S. Kragelund, A. Pongpunwattana, and B. Capozzi, "An evolution based path planning algorithm for autonomous motion of a UAV through uncertain environments," in *Proc. 21st Digital Avionics Syst. Conf.*, 2002, vol. 2, pp. 8D2-1–8D2-12.
[19] I. K. Nikolos, K. P. Valavanis, N. C. Tsourveloudis, and A. N. Kostaras, "Evolutionary algorithm based offline/online path planner for UAV navigation," *IEEE Trans. Syst., Man, Cybern. B, Cybern.*, vol. 33, no. 6, pp. 898–912, Dec. 2003.
[20] M. S. Branicky, S. M. LaValle, K. Olson, and Y. Libo, "Quasi-randomized path planning," in *Proc. IEEE ICRA*, 2001, vol. 2, pp. 1481–1487.
[21] J. Reif and Z. Sun, "Movement planning in the presence of flows," *Algorithmica*, vol. 39, no. 2, pp. 127–153, Feb. 2004.
[22] Z. Sun and J. Reif, "On robotic optimal path planning in polygonal regions with pseudo-Euclidean metrics," *IEEE Trans. Syst., Man, Cybern. B, Cybern.*, vol. 37, no. 4, pp. 925–936, Aug. 2007.
[23] N. A. Papadakis and A. N. Perakis, "Deterministic minimal time vessel routing," *Oper. Res.*, vol. 38, no. 3, pp. 426–438, May/Jun. 1990.
[24] J. Sellen, "Direction weighted shortest path planning," in *Proc. IEEE Int. Conf. Robot. Autom.*, May 1995, vol. 2, pp. 1970–1975.
[25] D. B. Fogel, *Evolutionary Computation: Toward a New Philosophy of Machine Intelligence*. San Francisco, CA: Morgan Kaufmann, 1995.
[26] RTCA, Software Considerations in Airborne Systems and Equipment Certification, 1992.
[27] G. F. List, P. B. Mirchandani, M. A. Turnquist, and K. G. Zografos, "Modeling and analysis for hazardous materials transportation—Risk analysis, routing scheduling and facility location," *Transp. Sci.*, vol. 25, no. 2, pp. 100–114, May 1991.
[28] P. B. Mirchandani and H. Soroush, "Optimal paths in probabilistic networks: A case with temporary preferences," *Comput. Oper. Res.*, vol. 12, no. 4, pp. 365–381, 1985.
[29] P. Leonelli, S. Bonvicini, and G. Spadoni, "Hazardous materials transportation: A risk-analysis-based routing methodology," *J. Hazardous Mater.*, vol. 71, no. 1–3, pp. 283–300, Jan. 2000.
[30] M. Zhang, Y. Ma, and K. Weng, "Location-routing model of hazardous materials distribution system based on risk bottleneck," in *Proc. Int. Conf. Services Syst. Services Manage.*, 2005, vol. 1, pp. 362–368.
[31] P. Wu, R. Clothier, D. Campbell, and R. Walker, "Fuzzy multi-objective mission flight planning in unmanned aerial systems," in *Proc. IEEE Symp. Comput. Intell. Multi-Criteria Decision-Making*, Honolulu, HI, 2007, pp. 2–9.
[32] B. S. Stewart, I. Chelsea, and C. White, "Multiobjective A*," *J. ACM*, vol. 38, no. 4, pp. 775–814, Oct. 1991.
[33] K. Erol, J. Hendler, and D.S. Nau, "HTN planning: Complexity and expressivity," in *Proc. AAAI Nat. Conf. Artif. Intell.*, 1994, pp. 1123–1128.
[34] P. Doherty, J. Gustafsson, L. Karlsson, and J. Kvarnstrom, "(TAL) Temporal action logics: Language specification and tutorial," *Electron. Trans. Artif. Intell.*, vol. 2, no. 3/4, pp. 273–306, 1998.
[35] A. Mali and Y. Lipen, "MFSAT: A SAT solver using multi-flip local search," in *Proc. IEEE Int. Conf. Tools Artif. Intell.*, Nov. 2003, pp. 84–93.
[36] T. Belker, M. Hammel, and J. Hertzberg, "Learning to optimize mobile robot navigation based on HTN plans," in *Proc. ICRA*, Sep. 2003, vol. 3, pp. 4136–4141.
[37] J. Bresenham, "Pixel-processing fundamentals," *IEEE Comput. Graph. Appl.*, vol. 16, no. 1, pp. 74–82, Jan. 1996.
[38] W. F. Phillips, *Mechanics of Flight*. Hoboken, NJ: Wiley, 2004.
[39] P. Wu, D. Campbell, and T. Merz, "On-board multi-objective mission planning for unmanned aerial vehicles," in *Proc. IEEE Aerosp. Conf.*, Big Sky, MT, Mar. 7–14, 2009, pp. 1–10.
[40] S. J. Russell and P. Norvig, *Artificial Intelligence: A Modern Approach*, 2nd ed. Upper Saddle River, NJ: Prentice-Hall, 2003.
[41] Civil Aviation Safety Authority (CASA), Civil Aviation Regulations 1988 (CAR 1988), Aug. 2003.
[42] D. Ferguson, M. Likhachev, and A. T. Stentz, "A guide to heuristic-based path planning," in *Proc. ICAPS*, Monterey, CA, 2005.
[43] Office of the Secretary of Defense, Unmanned Aircraft Systems Roadmap: 2005–2030, Tech. Rep., 2005.
[44] Structure and Dynamics of Supercell Thunderstorms, NOAA National Weather Service, 2004, [Online]. Available: http://www.crh.noaa.gov/lmk/soo/docu/supercell.php

Paul P.-Y. Wu (M'09) received the Ph.D. degree with a thesis on "Multi-Objective Mission Flight Planning in Civil Unmanned Aerial Systems" from the Queensland University of Technology (QUT), Brisbane, Australia, in 2009.

He is currently a Researcher with the Australian Research Centre for Aerospace Automation, QUT. He has worked on some projects, including the modeling of risk presented to population centers from overflight of aircraft and delivery of multimedia content to mobile phones. He is currently undertaking research on algorithms and architectures for unmanned-aerial-vehicle path planning and risk analysis.

Dr. Wu was a recepient of the Engineers Australia Queensland Division J. H. Curtis Award.

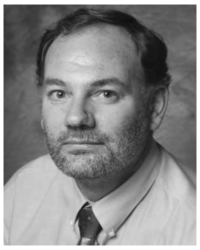

Duncan Campbell (M'84) received the Associate Diploma in electrical engineering from the Queensland Institute of Technology, Brisbane, Australia, and the B.S. degree (with honors) in electronics, physics, and mathematics and the Ph.D. degree from La Trobe University, Melbourne, Australia.

He is currently an Associate Professor with the Queensland University of Technology (QUT), Brisbane, Australia, where he is also the Alternate Head of the School of Engineering Systems. He is also currently a Group Leader with the Australian Research Centre for Aerospace Automation, Brisbane. He has collaborations with a number of universities around the world, including the Massachusetts Institute of Technology, Cambridge, and the TELECOM Bretagne, Brest, France. He has over 65 internationally peer-reviewed papers and research in the areas of robotics and automation, embedded systems, computational intelligence, intelligent control, and decision support.

Dr. Campbell is currently the IEEE Queensland Section Chapter Chair of the Control Systems/Robotics and Automation Society Joint Chapter.

Torsten Merz (M'09) received the Diploma degree in informatics from the University of Bielefeld, Bielefeld, Germany, and the D.E. degree from the University of Erlangen–Nuremberg, Erlangen, Germany.

He was an Assistant Professor with the Department of Computer and Information Science, Linköping University, Linköping, Sweden. He was with the Wallenberg Laboratory for Research on Information Technology and Autonomous Systems, Linköping University, where he was part of the unmanned-aerial-vehicle project team and involved in the development of flight modes and mission planners for unmanned helicopters. He is currently a Senior Research Scientist with the Autonomous Systems Laboratory, Commonwealth Scientific and Industrial Research Organisation, Brisbane, Australia. His research interests include dependable autonomous systems, unmanned aircraft systems, robot architectures, robot perception, and real-time systems.